Biodegradable MnO$_2$-based gene-engineered nanocomposites for chemodynamic therapy and enhanced antitumor immunity

Yiru Wang [a,b,1], Ming Wu [a,1], Xiaorong Wang [a,b,1], Peiyuan Wang [d], Zhaoyu Ning [a,b], Yongyi Zeng [a], Xiaolong Liu [a,d], Haiyan Sun [c,*], Aixian Zheng [a,**]

[a] The United Innovation of Mengchao Hepatobiliary Technology Key Laboratory of Fujian Province, Mengchao Hepatobiliary Hospital of Fujian Medical University, Fuzhou, 350025, PR China
[b] College of Biological Science and Engineering, Fuzhou University, Fuzhou, 350116, PR China
[c] Department of Anesthesiology, Beijing Anzhen Hospital, Capital Medical University, Beijing, 100029, PR China
[d] Key Laboratory of Design and Assembly of Functional Nanostructures, Fujian Institute of Research on the Structure of Matter, Chinese Academy of Sciences, Fuzhou, 350002, PR China

ABSTRACT

Immune checkpoint blockade (ICB) is emerging as a promising therapeutic approach for clinical treatment against various cancers. However, ICB based monotherapies still suffer from low immune response rate due to the limited and exhausted tumor-infiltrating lymphocytes as well as tumor immunosuppressive microenvironment. In this work, the cell membrane with surface displaying PD-1 proteins (PD1-CM) was prepared for immune checkpoint blockade, which was further combined with multifunctional and biodegradable MnO$_2$ for systematic and robust antitumor therapy. The MnO$_2$-based gene-engineered nanocomposites can catalyze the decomposition of abundant H$_2$O$_2$ in TME to generate O$_2$, which can promote the intratumoral infiltration of T cells, and thus improve the effect of immune checkpoint blockade by PD-1 proteins on PD1-CM. Furthermore, MnO$_2$ in the nanocomposites can be completely degraded into Mn^{2+}, which can catalyze the generation of highly toxic hydroxyl radicals for chemodynamic therapy, thereby further enhancing the therapeutic effect. In addition, the prepared nanocomposites possess the advantages of low cost, easy preparation and good biocompatibility, which are expected to become promising agents for combination immunotherapy.

1. Introduction

Cancer immunotherapy is considered to be one of the most promising therapeutic approaches that stimulating inherent immune system to eliminate cancer cells [1,2]. Among them, immune checkpoint blockade (ICB) has been of great interest due to its remarkable effect to various cancers. Programmed death-1 (PD-1)/programmed death-ligand 1 (PD-L1) pathway is one of the most important signaling pathways involved in tumor immune escape [3,4]. PD-1 is a transmembrane protein expressed on activated effector T cells, while PD-L1 is the ligand of PD-1 that is reported to be highly expressed on various cancer cells. The specific binding of PD-L1 on tumor cells to PD-1 on T cells can dramatically inhibit the function of T cells and thus lead to tumor immune evasion. On the other hand, blocking the interaction between PD-1 and

PD-L1 can restore the function of T cells and thus promote antitumor immune response [5–8]. Up to now, many antibody-based immune checkpoint inhibitors have been approved for the treatment of various malignancies, and the immune checkpoints include PD-1 and PD-L1 [9–11]. However, the antibodies for ICB need complicated preparation and isolation, which is laborious and expensive.

Cell membrane-based vesicles have attracted widespread attention in recent years, which hold great promise for biomedical applications owing to their easy preparation and good biocompatibility [12–18]. In addition, they can be endowed with more functions by means of genetic engineering [19–22]. For instance, this approach has been successfully applied to construct vesicles with surface displaying PD-1 proteins to block immune checkpoint for enhancing antitumor immune response [23,24]. Nevertheless, only a subset of cancer patients can benefit from

ICB monotherapies due to limited and exhausted tumor-infiltrating lymphocytes as well as tumor immunosuppressive microenvironment. Therefore, it is necessary to develop rational combination strategies for improving the therapeutic effect of ICB.

Compared with normal physiological conditions, the tumor microenvironment (TME) usually shows the typical features including mild acidic condition, hypoxia, vascular abnormalities and high levels of hydrogen peroxide (H_2O_2), which would promote tumor growth and metastases [25–28]. Tumor hypoxia is mainly caused by abnormal vascular structure and rapid proliferation of tumor cells in solid tumors, which is an extremely important factor that affects the efficacy of immunotherapy [27,29]. Recently, great efforts have been devoted to the development of efficient immunotherapeutic strategies by TME modulation [30–34]. Specially, abundant H_2O_2 in TME can be used as a good oxygen source, which can be converted into oxygen (O_2) under the action of catalase or its mimic enzymes, thus relieving tumor hypoxia and promoting T cell tumor infiltration.

Various types of nanostructured MnO_2 [35–37] have been recognized as a robust assistor to catalyze the decomposition of H_2O_2 into O_2, which can efficiently relieve tumor hypoxia to improve the effect of different treatments including chemotherapy, photodynamic therapy and immunotherapy [38–42]. On the other hand, MnO_2 can be completely degraded into Mn^{2+} that can be rapidly excreted by kidneys, thus avoiding long-term toxicity. It is reported that Mn^{2+} itself can promote the activation of cyclic GMP-AMP synthase (cGAS)/stimulator of interferon genes (STING) pathway and thus strengthen antitumor immune responses through the production of type I-interferon (IFN) [43,44]. It is worth mentioning that Mn^{2+} also exhibits the Fenton-like activity, which can catalyze the generation of hydroxyl radicals (·OH) in the presence of H_2O_2 and HCO_3^- that can cause oxidative damage to lipids, proteins, DNA and other biomolecules [45–47]. As well known, GSH is an important intracellular antioxidant that can react with the generated ·OH, thereby reducing the killing effect. In this case, the generation of Mn^{2+} from MnO_2 degradation can deplete endogenous GSH, and thus reduce its influence on Mn^{2+} based chemodynamic therapy.

Herein, the cell membrane with surface displaying PD-1 proteins (PD1-CM) was prepared by genetic engineering technology to perform the function of immune checkpoint blockade, which was further combined with hollow MnO_2 for systematic and robust antitumor effect through modulating TME. Due to the compelling functions of MnO_2, the prepared nanocomposites (MnO_2@PD1-CM) can catalyze the conversion of H_2O_2 in TME into O_2, which can promote the intratumoral infiltration of T cells, and thus improve the effect of PD1-CM based immune checkpoint blockade. In addition, Mn^{2+} produced by the degradation of MnO_2 also can catalyze the generation of highly toxic ·OH, which can further enhance the therapeutic effect. Furthermore, these biodegradable MnO_2-based gene-engineered nanocomposites should have good biocompatibility, which are expected to become promising therapeutic agents for various cancers.

2. Materials and methods

2.1. Reagents and apparatus

2′,7′-Dichlorodihydrofluorescein diacetate (DCFH-DA), Manganese nitrate tetrahydrate, 4′,6-Diamidino-2-phenylindole Dihydrochloride (DAPI) and glutathione (GSH) were obtained from Sigma-Aldrich Chemical Co. (USA). Triethanolamine was purchased from Shanghai Sangon Biotechnology Co. (China). Tetraethylorthosilicate was purchased from Absin Bioscience Inc (China). Coomassie Brilliant Blue G250 and 4% paraformaldehyde were purchased from Beijing Solarbio Technology Co., Ltd (China). Fluorescent probe DiO, BCA protein quantitation kit, membrane and cytosol protein extraction kit were purchased from Beyotime Biotechnology Co., Ltd. (China). Cell Count kit-8 (CCK8) was purchased from TransGen Biotech (China). Methylene blue (MB) was purchased from J&K Scientific Ltd (China). *Anti*-PD-1 antibody, *anti*-PD-

L1 antibody and *anti*-Ki67 antibody were purchased from Abcam (UK). Most of other reagents such as cyclohexane, sodium carbonate and phosphate were purchased from Sinopharm Chemical Reagent Co. Ltd. (China). Ultrapure water was obtained from Millipore water purification system.

The absorbance spectra were measured by a multifunctional microplate reader (Spectra Max M5, Molecular Devices). The particle size and zeta potential were estimated by Zetasizer Nano ZS (Malvern Instruments, UK) through dynamic light scattering (DLS). The confocal fluorescence images were recorded by a laser scanning fluorescence microscope (Zeiss LSM780). Flow cytometry analysis was performed by a FACSVerse BD flow cytometer. The analysis of serum biochemical indicators was performed by an automatic biochemical analyzer (CX5, Beckman, USA).

2.2. Cell culture

The mouse liver cancer cells (Hepa1-6), Chinese hamster ovary cells (CHO–S) and the constructed CHO-PD1 cells were cultured in DMEM medium containing 10% fetal bovine serum (FBS) and 1% penicillin/streptomycin at 37 °C in an incubator containing 5% CO_2.

2.3. Construction and identification of stable-expressing cells

The plasmid PCDH-CMV-PD1-mCherry-Puro encoding murine PD-1 as well as mCherry fused at its *C*-terminal was firstly constructed. Then, CHO–S cells were transformed by genetic engineering technology to obtain CHO-PD1 cells with high and stable PD-1 expression, in which PD-1 and mCherry were expressed in fusion. Briefly, the plasmid and lentiviral constructs were co-transfected into 293 F T cells using Lipofectamine 3000 Transfection Kit. The viral supernatants were harvested by ultracentrifugation at 25,000 rpm (4 °C) for 90 min. After purification and concentration, the lentivirus was stored at −80 °C for further use. To obtain stable-expressing CHO-PD1 cells, CHO–S cells were infected with the lentivirus and selected by 5 μg/mL puromycin. The expression of PD-1 on CHO–S cells can be verified by confocal imaging due to the red fluorescence from the fused mCherry. For this purpose, 3×10^5 CHO-PD1 cells were seeded in a 15 mm confocal dish. These cells were fixed with 4% paraformaldehyde for 10 min, and then stained with DAPI for 15 min as well as membrane fluorescent dye (DiO) for 10 min. After washing with PBS, the cells were imaged by a confocal microscope. The ratio of stable-expressing cells was analyzed by flow cytometry.

2.4. Western blot

The expression of PD-1 on CHO-PD1 cells can be further verified by western blot. Briefly, CHO–S and CHO-PD1 cells were lysed in RIPA lysis buffer containing 1% PMSF and 2% protease/phosphatase inhibitor (Cocktail). After complete lysis, the supernatant was collected after centrifugation at 17,000 g (4 °C) for 30 min, and then quantified through BCA protein quantitation kit. The equal protein samples were separated by polyacrylamide (10%) gel electrophoresis and then transferred to the NC membrane. After blocking, the NC membrane was incubated with *anti*-PD-1 antibody overnight, and then incubated with corresponding secondary antibody for 1 h. Finally, the expression of PD-1 was visualized by a Gel imaging system (Bio-Rad). Meanwhile, β-actin was selected as the reference protein.

2.5. Preparation and characterization of hollow MnO_2

The preparation process of hollow MnO_2 was as follows: 1.5 g of CTAB was added to 60 mL of water, and then 25% triethanolamine was added after 0.5 h. After further stirring for 0.5 h, 20% tetraethylorthosilicate dissolved in cyclohexane was added to the upper layer of the solution and reacted for 48 h. After that, the mixture was processed by centrifugation, and the obtained precipitate was further used as the

template to prepare hollow MnO_2. Briefly, 100 mg of the precipitate was dispersed in 60 mL of water, and then 0.212 g of manganese nitrate tetrahydrate was added to the solution. After stirring for 0.5 h, 0.15 g of urotropine was added and incubated for 4 h. After processed by centrifugation, the collected precipitate was further etched with 0.2 M sodium carbonate at 60 °C overnight to obtain hollow MnO_2. The morphology and size of hollow MnO_2 were verified by transmission electron microscopy (TEM). Meanwhile, the hydrodynamic size and zeta potential of them were determined by DLS.

2.6. Preparation and characterization of MnO_2@PD1-CM

CHO–S cells and CHO-PD1 cells were cultured in 10 cm dishes. The cells were collected by a scraper and were centrifuged at 800 g (4 °C) for 10 min. After washed with PBS for three times, the cells were incubated with membrane protein extraction reagent containing 10% PMSF for 30 min on ice. After that, the samples were quickly frozen in liquid nitrogen and then placed at room temperature until thawed. After repeating this process three times, the samples were centrifuged at 7000 rpm for 10 min to remove the precipitate. Then, the supernatant was further centrifuged at 40,000 g (4 °C) for 1 h. The resulting precipitate of cell membrane was re-suspended in PBS and stored at −80 °C for further use. Membrane proteins can be quantified by the BCA protein quantification kit.

For the preparation of MnO_2@PD1-CM, 1 mg/mL suspension of CHO-PD1 cell membrane (PD1-CM) was sonicated in an ice bath for 10 min. Subsequently, 400 μL of the above PD1-CM was mixed with 400 μL of 1 mg/mL MnO_2 solution under sonication for 5 min, and then passed through the polycarbonate membranes with pore diameters of 1000 nm and 400 nm in turn for 11 times. Then, the PD1-CM coated MnO_2 (MnO_2@PD1-CM) was obtained and stored at 4 °C for further use. The synthesized nanocomposites were characterized by absorption spectra, TEM imaging, DLS analysis, and so on. The proteins in PD1-CM and MnO_2@PD1-CM can be characterized by Coomassie brilliant blue staining. The samples were separated by 10% SDS-PAGE gel electrophoresis, and then stained with G250 Coomassie brilliant blue for 2 h. After destaining, the gel was visualized by a Gel imaging system (Bio-Rad).

2.7. Immunoprecipitation assay

The orientation of PD-1 protein on PD1-CM or MnO_2@PD1-CM was verified by immunoprecipitation assay. Briefly, 100 μL of protein A/G magnetic bead was washed with PBS and further mixed with 2 μL of 1 mg/mL *anti*-PD-1 antibody and 400 μL of 1 mg/mL PD1-CM or MnO_2@PD1-CM (concentration based on membrane protein). After incubation overnight at 4 °C, the collected magnetic beads were washed three times with PBS and then subjected to western blot analysis. As a control, the *anti*-PD-1 antibody was replaced with IgG, and the same procedure was performed.

2.8. The degradation of MnO_2 into Mn^{2+}

The degradation of MnO_2 can be mediated by GSH, and this reaction can be verified by absorption spectrum and inductively coupled plasma atomic emission spectrometer (ICP-OES). Briefly, 200 μL of 4 mg/mL MnO_2 solution was mixed with 100 μL of 100 mM GSH and 700 μL of 10 mM PBS (pH = 6.7) for 20 min. Then, the absorption spectra of MnO_2 with or without GSH treatment were measured by a multifunctional microplate reader. For the analysis of Mn^{2+}, the solution with or without GSH treatment were centrifuged at 12,000 g for 10 min to remove the precipitate. After passing through 0.22 μm filter, the concentration of Mn^{2+} in the solution was detected by ICP-OES.

When verified at cellular level, Hepa1-6 cells were seeded in a 6-well plate with a density of 3×10^5 cells per well, then were respectively incubated with 2 mL of PBS and MnO_2@PD1-CM (80 μg/mL) for 12 h. After that, the treated cells were collected and broken by ultrasound. The obtained mixture was centrifuged at 12,000 g for 10 min to remove the

precipitate, and the concentration of Mn^{2+} in the supernatant was measured by ICP-OES to verify the degradation of MnO_2 into Mn^{2+}.

2.9. Catalytic generation of hydroxyl radicals

The generation of ·OH can be verified by the degradation of methylene blue (MB). Briefly, 1 mg/mL MnO_2 solution was mixed with 10 mM GSH in 25 mM $NaHCO_3$ solution for 15 min, and then centrifuged at 12,000 g for 10 min. Subsequently, 40 μL of the supernatant was incubated with 30 μg/mL MB and 10 mM H_2O_2 at 37 °C for 1 h. Finally, the absorption spectrum of the solution in the range from 500 nm to 800 nm was measured.

To verify intracellular ·OH generation, Hepa1-6 cells were seeded in a 96-well plate with a density of 1×10^4 cells per well, followed by incubation with PBS, PD1-CM, MnO_2 and MnO_2@PD1-CM (80 μg/mL), respectively. After incubation for 2 h, 40 μM of DCFH-DA was added and then incubated for another 30 min. Finally, the cells were washed twice with PBS and then imaged by a confocal microscope to verify the generation of hydroxyl radicals.

2.10. CCK-8 assay

The antitumor effect of PD1-CM, MnO_2 and MnO_2@PD1-CM to Hepa1-6 cells was evaluated by a cell counting kit (CCK-8). Briefly, Hepa1-6 cells were seeded in a 96-well plate with a density of 1×10^4 cells per well, and then incubated with different concentrations of PD1-CM, MnO_2 or MnO_2@PD1-CM (0, 4, 8, 10, 20, 40, 80 μg/mL) for 24 h. After washed three times with PBS, 100 μL of fresh medium containing 10% CCK-8 solution was added to each well and then incubated in a 37 °C incubator containing 5% CO_2 for 1 h. Finally, the absorbance of the solution at 450 nm was measured by a multifunctional microplate reader to evaluate the cell viability.

2.11. Confocal imaging

For imaging purposes, CHO-CM and PD1-CM were incubated respectively with DiO at room temperature for 30 min, and then centrifuged at 40,000 g to remove the unbound DiO. Meanwhile, Hepa1-6 cells were seeded in a 15 mm confocal dish at a density of 3×10^5 per well. After that, 100 μg/mL of DiO-labelled CHO-CM, PD1-CM or MnO_2@PD1-CM were added and incubated at 37 °C for 2 h. After fixed with 4% paraformaldehyde for 15 min, the cells were stained with DAPI for 15 min and then observed under a confocal fluorescence microscope.

To illustrate the interaction of prepared MnO_2@PD1-CM to PD-L1 on Hepa1-6 cells, the cells were seeded in a 15 mm confocal dish, and then pre-treated with *anti*-PD-L1 antibody for 2 h. After that, 100 μg/mL of DiO-labelled MnO_2@PD1-CM were added and incubated at 37 °C for 2 h. After fixed with 4% paraformaldehyde for 15 min, the cells were stained with DAPI for 15 min and then observed under a confocal fluorescence microscope.

2.12. In vivo antitumor effect of MnO_2@PD1-CM

Male C57BL/6 mice were purchased from China Wushi, Inc. (Shanghai, China). All animal experiments were approved by the Animal Ethics Committee of Mengchao Hepatobiliary Hospital of Fujian Medical University. Firstly, tumor-bearing mice were constructed by subcutaneously injecting 3×10^6 Hepa1-6 cells into each mouse. When tumor volume reached 80–100 mm^3, they were randomly divided into four groups with 8 mice in each group. Then, 50 μL of PBS, PD1-CM, MnO_2@CHO-CM or MnO_2@PD1-CM (100 μg membrane proteins) were intratumorally injected into tumor-bearing mice of each group on days 1, 4, 7, and 10, respectively. During this process, the tumor volume and body weight of each mouse were monitored every two days. Tumor volume was measured by a Vernier caliper, and was calculated to be $LW^2/2$, where L was the longest diameter of tumor and W was the

shortest diameter of tumor. The mouse was euthanized when its tumor volume reached 1200 mm^3.

For the assessment of antitumor effect and biosafety, three mice in each group were sacrificed on the fourth day after last injection. Then, the tumors and major organs (heart, liver, spleen, kidney and lung) were fixed in formalin solution, and were embedded in paraffin. The tumor

sections were deparaffinized and then subjected to hematoxylin-eosin (H&E) staining, Ki67 staining and other immunofluorescence staining analysis. For Ki67 staining, the tumor sections were blocked with BSA, and then incubated with Ki67 antibody as well as the HRP-labelled secondary antibody. After incubated with DAB staining solution, the tumor sections were immersed in hematoxylin for counterstaining, and then
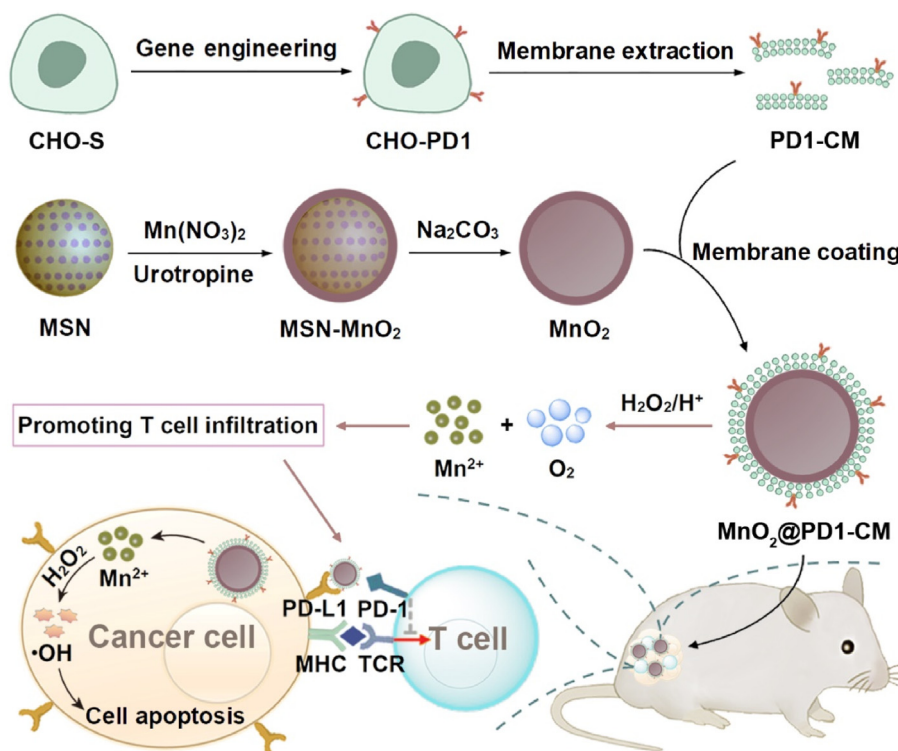

Fig. 1. Schematic illustration of the preparation of MnO$_2$@PD1-CM nanocomposites and their application in antitumor therapy.
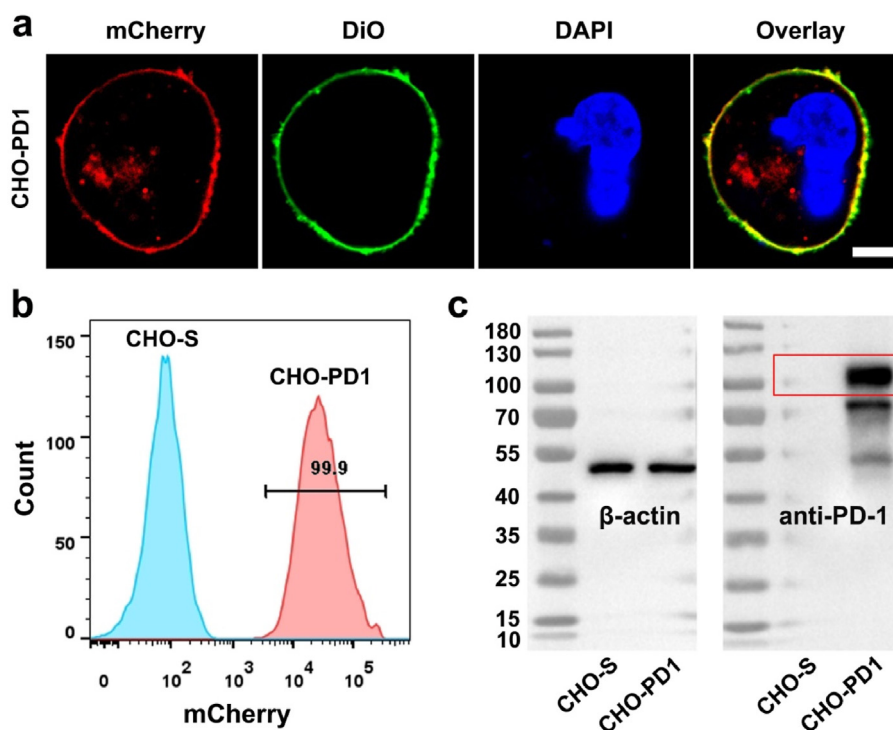

Fig. 2. (a) Confocal images of the co-localization of fusion protein PD-1-mCherry and DiO-labelled cell membrane. Scale bar: 5 μm; (b) flow cytometry analysis of mCherry positive rate of CHO-PD1 cells; (c) western blot analysis of PD-1 expression on CHO–S and CHO-PD1 cells, and β-actin was used as control.

placed under an optical microscope for observation. For immunofluorescence staining of HIF-1α, CD4 or CD8, the tumor sections were incubated with the corresponding antibodies and fluorescent secondary antibodies after blocking with BSA. Finally, each tumor section was covered with a coverslip and placed under a confocal fluorescence microscope for observation.

Meanwhile, a portion of the tumor from each group was collected and digested with 0.2 mg/mL hyaluronidase, 1 mg/mL collagenase IV and 0.02 mg/mL DNase I at 37 °C for 1 h. After filtration, the cells were collected by centrifugation at 800g for 5 min, and purified by red blood cell lysate as well as Ficoll-based density gradient centrifugation at 800g for 20 min. The collected single cell suspension was firstly blocked with BSA, and then stained with anti-CD3-APC, anti-CD4-FITC and anti-CD8-PE antibodies for flow cytometry analysis. Moreover, a portion of the tumor from each group was homogenized with 1 mL PBS by an automatic sample rapid grinding machine for the analysis of IFN-γ and TNF-α. The supernatant was collected by centrifugation at 12,000 rpm for 10 min,

and then the corresponding cytokine levels were detected by ELISA kits.

2.13. Biosafety assessment

For biosafety assessment, the collected heart, liver, spleen, lung and kidney from the mice in each group were fixed in formalin solution, and were embedded in paraffin. After deparaffinization, the corresponding tissue sections were subjected to H&E staining, and then observed by an optical microscope. Moreover, the blood specimens of three mice in each group were collected for biochemical examination on the fourth day after last injection. After standing at 4 °C for 30 min, the serum was collected by centrifugation at 7000 rpm, and the serum biochemical indicators were detected through an automatic biochemical analyzer (CX5, Beckman, USA). The indicators included alanine aminotransferase (ALT), aspartate aminotransferase (AST), creatinine (CRE) and blood urea nitrogen (BUN) (see Fig. 1).
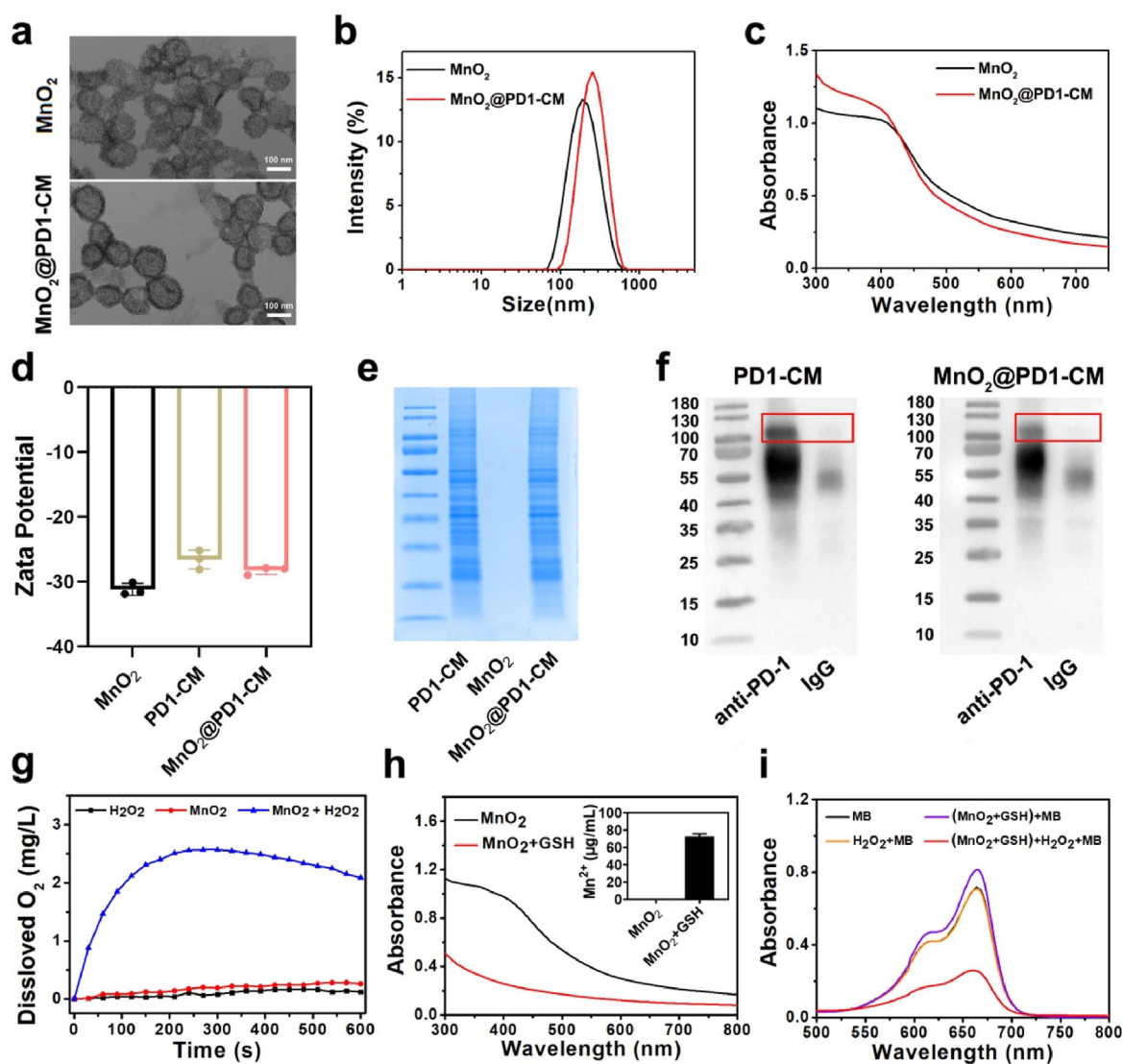

Fig. 3. (a) TEM images, (b) hydrodynamic size analysis and (c) absorption spectra of MnO_2 and MnO_2@PD1-CM; (d) zeta potential and (e) Coomassie brilliant blue staining of PD1-CM, MnO_2 and MnO_2@PD1-CM; (f) immunoprecipitation and western blot analysis to examine the orientation of PD-1 on PD1-CM and MnO_2@PD1-CM; (g) oxygen generation from the reaction of MnO_2 with H_2O_2 in 10 mM PBS buffer (pH = 6.5); (h) absorption spectra of MnO_2 and the solution after reacted with 10 mM GSH, the insert was the concentration of Mn^{2+} in corresponding solution; (i) absorption spectra of methylene blue (MB) after reacted with H_2O_2 or GSH-treated MnO_2.

3. Results and discussion

3.1. Construction and identification of CHO-PD1 cells

CHO–S cells with surface stably expressing PD-1 proteins (PD1-CM) were prepared by genetic engineering technology. To verify the stable expression of fused PD-1-mCherry on CHO–S cells, the cells were labelled with DiO (a lipophilic fluorescent probe that can bind to cell membranes). As shown in Fig. 2a, the red fluorescence signal of mCherry on the constructed CHO-PD1 cells was quite obvious. This phenomenon can prove the successful expression of PD-1-mCherry on CHO–S cells. Meanwhile, a large overlap of mCherry and DiO fluorescence was observed, further indicating the successful expression of PD-1-mCherry on the cell membrane. In addition to cell surface, red fluorescence was also observed in the cytoplasm. This is because that the proteins were synthesized in the cytoplasm and then transferred to the cell membrane.

Moreover, flow cytometry was used to detect the mCherry positive ratio of CHO-PD1 cells to verify the stable expression of fused PD-1-mCherry. As shown in Fig. 2b, the positive ratio of CHO-PD1 cells kept above 99.9% even being passaged for 6 generations, indicating that PD-1-mCherry could be stably expressed on CHO-PD1 cells. The successful expression of fused PD-1-mCherry was also verified by WB analysis. As shown in Fig. 2c, compared with parent cell, a new protein that can bind to PD-1 antibody was expressed on CHO-PD1 cells. However, its molecular weight was significantly larger than that of PD-1 recombinant protein provided by Abcam, verifying the fusion of PD-1 and mCherry in CHO-PD1 cells. All these results proved the successful expression of PD-1-mCherry on CHO-PD1 cells.

3.2. Preparation and characterization of MnO$_2$@PD1-CM

Hollow MnO$_2$ were synthesized by using mesoporous silica as template and then etched by sodium carbonate, which were further coated with PD1-CM for antitumor therapy. As shown in Fig. 3a, the TEM image can confirm that the synthesized MnO$_2$ nanomaterials were hollow and the size of which was in the range from 80 nm to 100 nm. Meanwhile, the average hydrodynamic size of hollow MnO$_2$ was about 184 nm (Fig. 3b). The synthesized hollow MnO$_2$ had a relatively broad absorbance around 400 nm, which is consistent with the absorption spectrum of MnO$_2$ reported in the previous literature [41,48], further proving the successful synthesis of hollow MnO$_2$ (Fig. 3c). After coating with cell membrane, a thin film could be observed on the surface of MnO$_2$@PD1-CM (Fig. 3a), and its average hydrodynamic size increased to 200.4 nm. As shown in Fig. 3d, the surface potential of MnO$_2$ was -31.2 ± 1.1 mV. After coating, the surface potential changed to -28.3 ± 0.7 mV, which was closer to that of PD1-CM. Moreover, coomassie brilliant blue staining confirmed that the protein in MnO$_2$@PD1-CM was almost the same as that in PD1-CM (Fig. 3e). These results can indirectly prove the successful encapsulation of MnO$_2$ by PD1-CM.

To exert the function of immune checkpoint blockade by PD-1 proteins, an important prerequisite is the right outward orientation of PD-1 proteins on the prepared MnO$_2$@PD1-CM to guarantee effectively binding to PD-L1 on the surface of cancer cells. We verified it by immunoprecipitation assay. In which, the protein A/G on the magnetic beads could bind to the Fc segment of *anti*-PD1 antibody, and then this antibody was used to capture PD-1 protein on the membrane. The data shown in Fig. 3f demonstrated that PD-1 protein on MnO$_2$@PD1-CM had the outward orientation and can bind to *anti*-PD1 antibody, which further
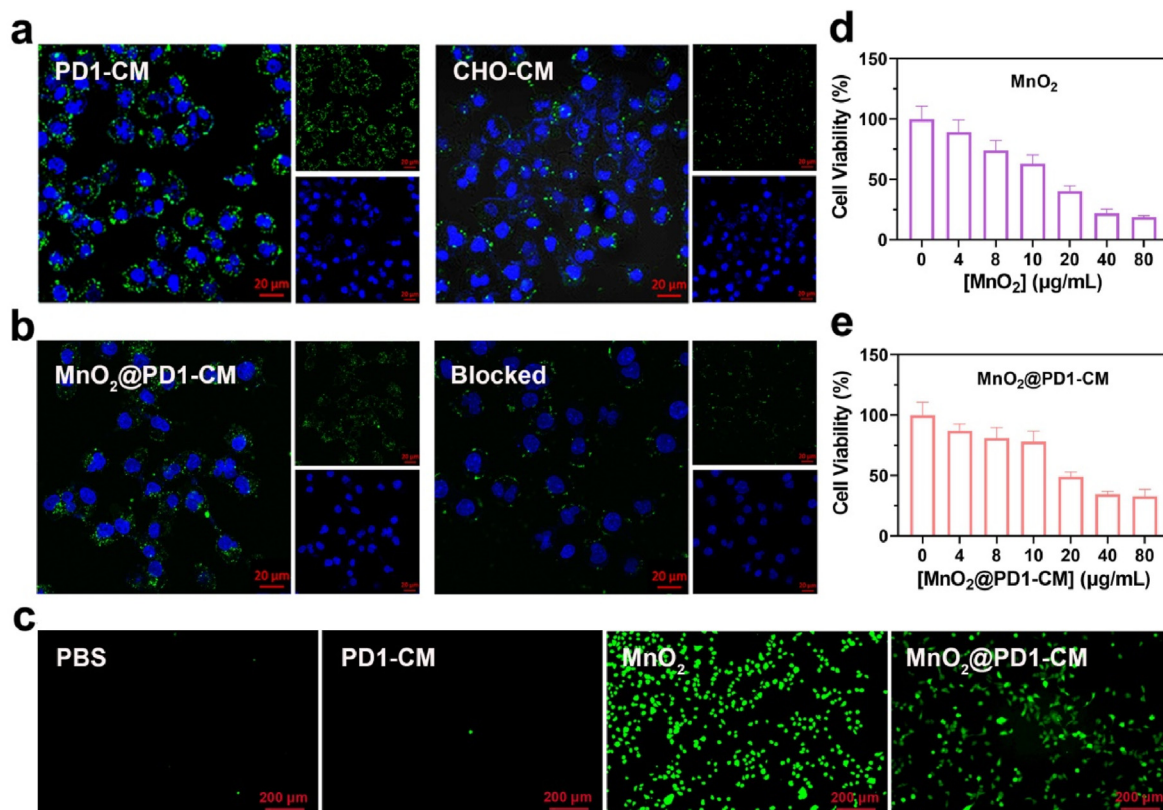

Fig. 4. (a) Confocal images of Hepa1-6 cells after incubated with DiO-modified PD1-CM or CHO-CM. Scale bar: 20 μm; (b) confocal images of Hepa1-6 cells and *anti*-PD-L1 antibody pre-treated Hepa1-6 cells after incubated with DiO-modified MnO$_2$@PD1-CM, Scale bars: 20 μm; (c) DCFH-DA indicating the production of intracellular ROS in Hepa1-6 cells after treated with PD1-CM, MnO$_2$ or MnO$_2$@PD1-CM; cell viability of Hepa1-6 cells after treated with different concentrations of MnO$_2$ (d) or MnO$_2$@PD1-CM (e) for 24 h.

indicated that the PD-1 proteins on MnO$_2$@PD1-CM might also bind to PD-L1 on cancer cells, thereby exert its biological function.

Since MnO$_2$ has been reported to possess the catalytic activity like catalase (CAT) to catalyze H$_2$O$_2$ into O$_2$ and thus relieve intratumor hypoxia, we next investigated this property though a portable dissolved oxygen meter. As shown in Fig. 3g, MnO$_2$ or H$_2$O$_2$ alone could not induce oxygen generation. When MnO$_2$ and H$_2$O$_2$ were mixed together, significant oxygen generation was observed and the amount of generated O$_2$ was related to their concentrations (Fig. S1). This result can confirm the catalase-like catalytic activity of MnO$_2$, which is expected to catalyze H$_2$O$_2$ in TME to generate O$_2$, thereby relieving tumor hypoxia and promoting T cell infiltration.

MnO$_2$ is biodegradable in vivo and thus also has the ability to deliver Mn^{2+} for chemodynamic therapy. As shown in Fig. 3h, the absorption spectrum of MnO$_2$ changed significantly after reaction with GSH, and its absorption around 400 nm was disappear, indicating that MnO$_2$ was degraded by reacting with GSH. Meanwhile, the concentrations of Mn^{2+} in the MnO$_2$ solution before and after reaction with GSH were measured by ICP-OES. As shown in the insert of Fig. 3h, the concentration of Mn^{2+} in the MnO$_2$ solution significantly increased after reaction with GSH, indicating the degradation of MnO$_2$ into Mn^{2+}. We further investigated the Fenton-like activity of Mn^{2+} degraded from MnO$_2$, which can catalyze the generation of ·OH for chemodynamic therapy. It is worth mentioning that methylene blue (MB) can be degraded into colorless product by ·OH, which can be used as an indicator of ·OH generation. As shown in Fig. 3i, when H$_2$O$_2$ and GSH-treated MnO$_2$ were added simultaneously, the absorbance of MB solution was significantly decreased. This suggested that MnO$_2$ can be degraded into Mn^{2+} and further catalyze the generation of ·OH for exerting antitumor effect.

3.3. The binding of nanocomposites to cancer cells

It is well known that PD1 protein on the surface of T cells can bind to PD-L1 on the surface of cancer cells, thereby causing tumor immune escape. To investigate whether PD1-CM immobilized on MnO$_2$ is able to interact with PD-L1 on cancer cells, the cell membrane based nanocomposites were stained with DiO, while the nuclei of Hepa1-6 cells were stained with DAPI. As shown in Fig. 4a, the green fluorescent signal in Hepa1-6 cells incubated with PD1-CM was much higher than that in cells incubated with CHO-CM, which means that PD-1 on PD1-CM can promote its binding to Hepa1-6 cells. Meanwhile, PD1-CM can still bind to Hepa1-6 cells after coating on the surface of MnO$_2$. As shown in Fig. 4b, when Hepa1-6 cells were incubated with MnO$_2$@PD1-CM, obvious green fluorescence can be observed and its fluorescence intensity was slightly weaker than that of cells incubated with PD1-CM, which may be because MnO$_2$ could quench DiO fluorescence to some extent. To further verify that the binding occurred through the interaction between PD-1 and PD-L1, Hepa1-6 cells were pre-treated with *anti*-PD-L1antibody and then incubated with DiO-modified MnO$_2$@PD1-CM for confocal imaging. As shown in Fig. 4b, the green fluorescence signal was significantly reduced after blocking, which indicated that MnO$_2$@PD1-CM can bind to cancer cells through the interaction between PD-1 and PD-L1, with great potential to block the immune checkpoints and thus enhance therapeutic efficacy.

3.4. Antitumor effect of MnO$_2$@PD1-CM at cellular level

DCFH-DA is a cell-permeable fluorescent probe for the detection of intracellular reactive oxygen species (ROS). After enters the cell, the
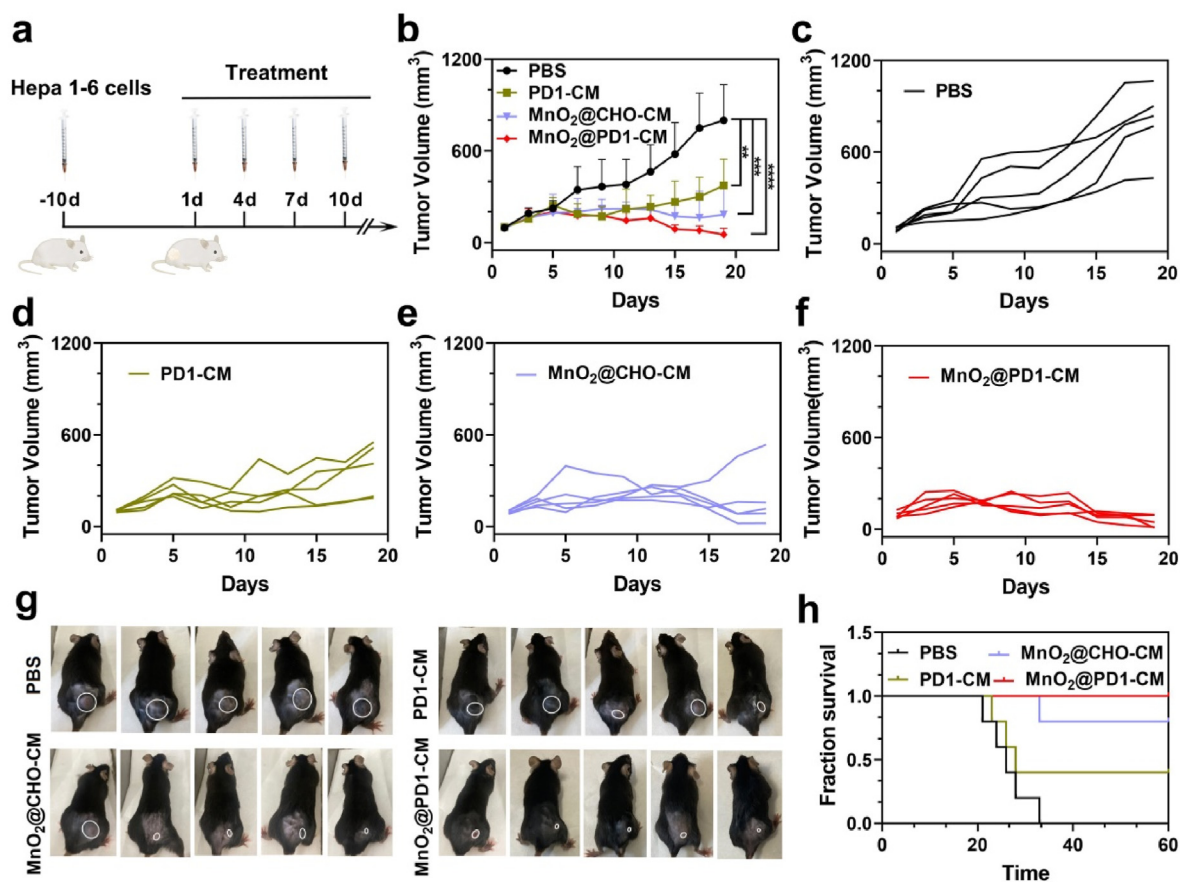

Fig. 5. **(**a) Schematic illustration of the treatment; (b–f) tumor growth curves of tumor-bearing mice after the treatment of PBS, PD1-CM, MnO$_2$@CHO-CM or MnO$_2$@PD1-CM; (g) photographs of the mice in each group when the tumor volume for one of the mice reached 1200 mm^3; (h) survival curves of the mice in each group.

probe will be deacetylated by cellular esterase to form 2′, 7′-dichloro-fluorescein (DCFH), and further oxidized into 2′,7′-dichlorofluorescein (DCF) with green fluorescence by intracellular ROS. When Hepa1-6 cells were incubated with MnO_2@PD1-CM, the concentration of Mn^{2+} in cell lysate increased significantly, indicating that MnO_2 can be degraded into Mn^{2+} in cells (Fig. S2). To verify the intracellular generation of ·OH, Hepa1-6 cells were firstly incubated with different nanocomposites, and then incubated with DCFH-DA for confocal fluorescence imaging. As shown in Fig. 4c, the green fluorescence of Hepa1-6 cells in MnO_2 group was significantly higher than that in PBS and PD1-CM group, indicating that the endogenous ROS level was relatively low and MnO_2 can induce the generation of ROS. This may be attributed to the intracellular degradation of MnO_2 into Mn^{2+}, and thus catalyze the conversion of endogenous H_2O_2 into more reactive ·OH that can kill tumor cells. Obvious green fluorescence was also observed in the MnO_2@PD1-CM group, indicating that MnO_2 can still induce the conversion of endogenous H_2O_2 into ·OH after coating the PD1-CM. There was a slight decrease in green fluorescence, which may be because the PD1-CM coating could reduce the reaction rate of MnO_2 in the nanocomposites [49].

To further illustrate the antitumor effect of MnO_2@PD1-CM, Hepa1-6 cells were incubated with different concentrations of MnO_2@PD1-CM for 24 h, and then the cell viability was evaluated by CCK-8. Meanwhile, MnO_2 and PD1-CM were used as control. As shown in Fig. 4d, MnO_2 had

a significant influence on cell survival. As the MnO_2 concentration increased to 80 μg/mL, the cell viability decreased to 18.3%. PD1-CM had no significant influence on cell survival (Fig. S3). Nevertheless, the cell viability in MnO_2@PD1-CM group was similar to that in MnO_2 group. Compared with MnO_2 group, the cells treated with MnO_2@PD1-CM had a slightly higher survival rate (Fig. 4e), which may be ascribed to the decrease of reaction rate after coating with PD1-CM. But they still had a strong antitumor effect on Hepa1-6 cells. It is worth mentioning that the degradation of MnO_2 can deplete endogenous GSH, and thus enhance the killing effect caused by intracellular catalytic reaction. The nanocomposites may also have a certain impact on the survival of T cells. Increasing the accumulation of the nanocomposites at the tumor site may reduce this influence.

3.5. In vivo antitumor effect of MnO_2@PD1-CM

To evaluate the antitumor effect of MnO_2@PD1-CM in vivo, tumor-bearing mice were firstly constructed by subcutaneously injecting Hepa1-6 cells, and then randomly divided into four groups for different treatments. During the treatments, the tumor volume and body weight of each mouse were monitored every two days. The tumor growth curves of tumor-bearing mice after different treatments were summarized in Fig. 5b–f. It can be found that the tumor growth in PD1-CM, MnO_2@-CHO-CM and MnO_2@PD1-CM groups was significantly slower than that
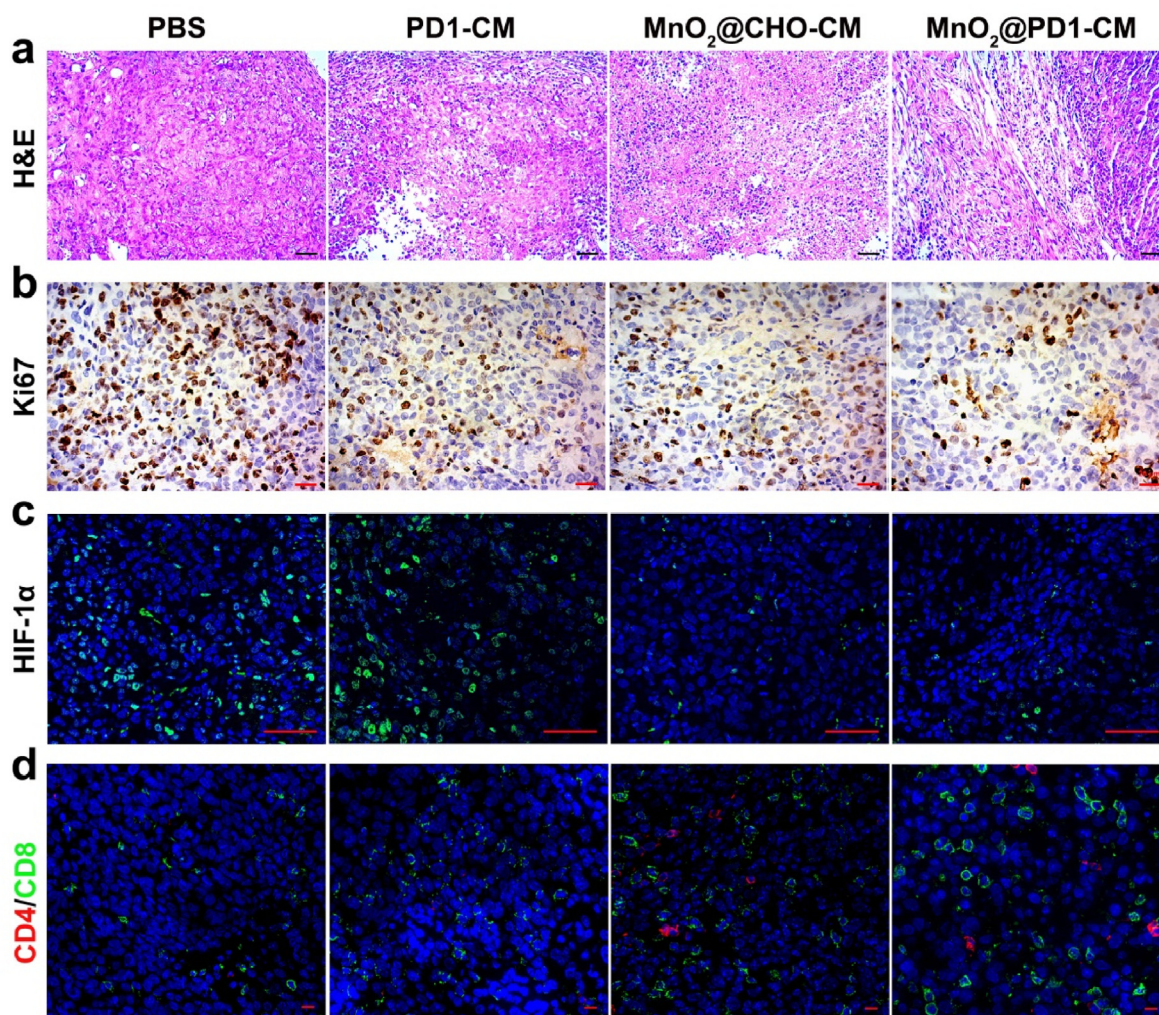

Fig. 6. (a) H&E and (b) Ki67 staining of tumor slices from different treatments. Scale bars were 20 μm and 50 μm, respectively; (c) immunofluorescence staining of HIF-1α in tumor slices from different treatments. Nuclei stained with DAPI were blue and the stained HIF-1α was green. Scale bar: 50 μm; (d) immunofluorescence staining of CD4 and CD8 in tumor slices from different treatments. Scale bar: 20 μm.

in PBS group. At the same time, MnO$_2$@PD1-CM exerted the best anti-tumor effect, which may due to the synergistic effect between MnO$_2$ and PD1-CM. In order to assess the antitumor effect more intuitively, all mice were photographed when the tumor volume for one of the mice reached 1200 mm^3. As shown in Fig. 5g, the tumors in PBS group were relatively large, and the tumors in MnO$_2$@CHO-CM and MnO$_2$@PD1-CM groups were significantly reduced. Especially in the MnO$_2$@PD1-CM group, it was difficult to find the protruding tumor from the photographs, which suggested that MnO$_2$@PD1-CM could better inhibit tumor growth. We also monitored the survival of the mice for up to 60 days. As shown in Fig. 5h, the survival time of the mice after the treatment of MnO$_2$@PD1-CM was significantly prolonged. Moreover, the body weight of the mice did not change significantly during the treatment (Fig. S4), indicating that these cell membrane-based nanocomposites had no obvious influence on the mice themselves.

We next assessed the antitumor effect of MnO$_2$@PD1-CM by immu-nofluorescence and immunohistochemically staining. For H&E staining, the PBS group had the most complete cell morphology, while the structures of tumor cells in PD1-CM, MnO$_2$@CHO-CM and MnO$_2$@PD1-CM group all suffered a certain degree of damage (Fig. 6a). Ki67 is expressed in the interphase of cell mitosis, which can be used as a marker for cell proliferation. As shown in Fig. 6b, the positive rate of Ki67 was decreased in different treatment groups, especially in MnO$_2$@PD1-CM group. This indicated that MnO$_2$@PD1-CM could effectively reduce tumor cell proliferation, thereby inhibiting tumor growth. PD1-CM and MnO$_2$@CHO-CM also exhibited a certain degree of antitumor effect, which may be due to the immune checkpoint blockade of PD-1 proteins as well as the chemodynamic therapy of Mn^{2+} generated by MnO$_2$ degradation. Possibly due to the synergistic effect of PD1-CM and MnO$_2$, MnO$_2$@PD1-CM exhibited a most efficient antitumor effect. Moreover, MnO$_2$ has been verified to catalyze the production of O$_2$, which was expected to relieve tumor hypoxia and promote the intratumoral infiltration of T cells [39, 50], thereby further enhancing the therapeutic effect.

Hypoxia-inducible factor 1α (HIF-1α) is ubiquitous in mammals and is easily degraded by ubiquitination. However, the ubiquitination of HIF-1α is affected under hypoxia, resulting in increased intracellular expression. Therefore, the expression of HIF-1α can indicate the level of tumor hypoxia. To investigate the effect of MnO$_2$@PD1-CM on relieving tumor hypoxia, immunofluorescence analysis of HIF-1α was performed on tumor sections after different treatments, and the green fluorescence could indicate the expression of HIF-1α. As shown in Fig. 6c, the green fluorescence was obvious in PBS and PD1-CM group, while almost no green fluorescence could be observed in MnO$_2$@CHO-CM and MnO$_2$@PD1-CM group. The decreased expression of HIF-1α indicated that MnO$_2$ in MnO$_2$@CHO-CM and MnO$_2$@PD1-CM could catalyze the generation of O$_2$ in TME, and thus relieve tumor hypoxia.

We next investigated the intratumoral infiltration of T cells after different treatments. On the fourth day after last injection, three mice from each group were sacrificed to prepare single cell suspension for flow cytometry analysis. Compared to PBS group, the percentages of CD8$^+$ and CD4$^+$ T cells in the tumors after different treatment were obviously increased (Fig. S5). Furthermore, the percentage of CD8$^+$ T cells in MnO$_2$@PD1-CM group was about 54.3%, which was obviously higher than that in PBS group (34.2%), indicating that MnO$_2$@PD1-CM could cause more CD8$^+$ T cells to infiltrate in the tumor. We further verified the infiltration of T cells by immunofluorescence staining, and the result was shown in Fig. 6d. It can be found that the numbers of intratumoral CD8$^+$ and CD4$^+$ T cells in the MnO$_2$-based experimental groups were significantly higher than those in PBS group, especially in MnO$_2$@PD1-CM group. Cytokine levels in the tumors of the treated mice were also analyzed by ELISA. Compared with PBS group, the levels of IFN-γ and TNF-α in the treated groups were obviously higher (Fig. S6). In general, the prepared MnO$_2$@PD1-CM could relieve tumor hypoxia and promote the intratumoral infiltration of T cells, thereby exerting a better anti-tumor effect.

3.6. Biosafety assessment

We finally evaluated the biosafety of the prepared MnO$_2$@PD1-CM by serum biochemical analysis and H&E staining. On the fourth day after last injection, the serums from three mice of each group were collected for the analysis of liver and kidney function indicators, such as ALT, AST, CRE and BUN. As shown in Fig. 7, there were no significant differences between PBS group and MnO$_2$@PD1-CM group. Meanwhile, the heart, liver, spleen, lung and kidney of the mice in PBS and MnO$_2$@PD1-CM group were also collected for H&E staining analysis. As shown in Fig. S7,
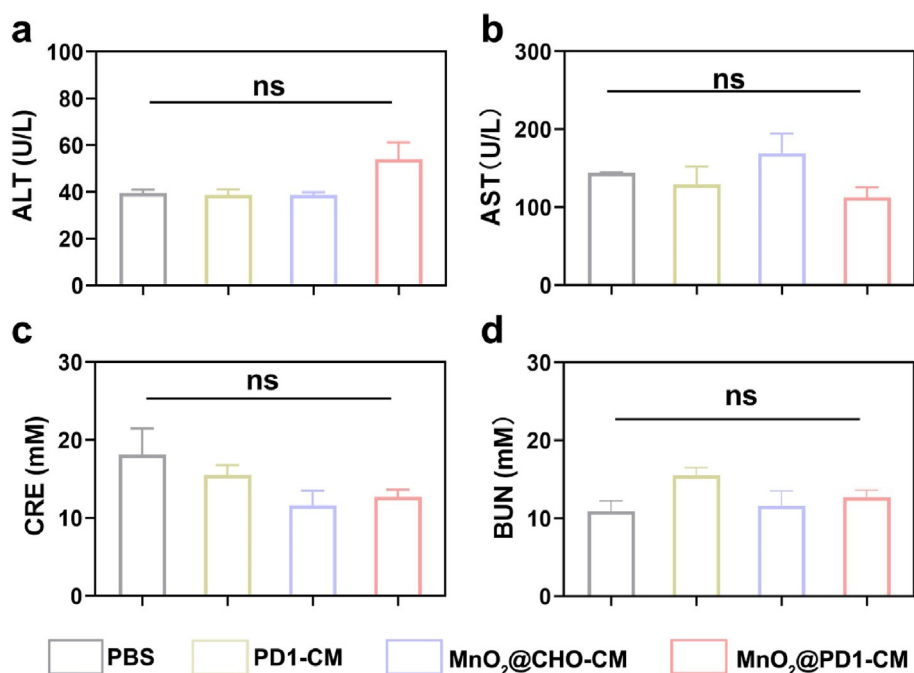

Fig. 7. The analysis of (a) ALT, (b) AST, (c) CRE and (d) BUN in serum from the mice with indicated treatments on the fourth day after last injection. N = 3.

MnO$_2$@PD1-CM did not cause obvious organ damage that was compared with PBS group, further proving the good biosafety of the prepared MnO$_2$@PD1-CM.

4. Conclusions

In general, in order to solve the problem of low response rate of immune checkpoint blockade, hollow MnO$_2$ and the cell membrane with surface displaying PD-1 proteins were used to construct the multifunctional MnO$_2$@PD1-CM for systematic and robust antitumor therapy. The prepared nanocomposites can catalyze the decomposition of H$_2$O$_2$ in TME into O$_2$, thus alleviating the tumor hypoxia microenvironment. In this way, the intratumoral infiltration of T cells can be promoted, thus enhancing the effect of immune checkpoint blockade by PD-1 proteins on PD1-CM. In addition, the nanocomposites can catalyze the generation of highly toxic ·OH for chemodynamic therapy, thereby further enhancing the therapeutic effect. We have successfully verified that the prepared MnO$_2$@PD1-CM can specifically bind to PD-L1 on the surface of cancer cells, and its antitumor effect has been verified at cellular and animal levels. Moreover, these nanocomposites possess the advantages of easy preparation, low cost and good biocompatibility, which are expected to provide new ideas for systematic immunotherapy.

Author contributions

Yiru Wang: Methodology, Investigation, Formal analysis, Visualization, Writing – original draft; Ming Wu: Methodology, Investigation, Writing – review & editing; Xiaorong Wang: Methodology, Investigation, Formal analysis; Peiyuan Wang: Investigation; Zhaoyu Ning: Investigation; Yongyi Zeng: Supervision, Funding acquisition; Xiaolong Liu: Supervision, Funding acquisition; Haiyan Sun: Project administration, Funding acquisition, Writing – review & editing; Aixian Zheng: Conceptualization, Project administration, Funding acquisition, Writing – review & editing.

Declaration of competing interest

The authors declare that they have no known competing financial interests or personal relationships that could have appeared to influence the work reported in this paper.

Data availability

Data will be made available on request.

Acknowledgements

Appendix A. Supplementary data

Supplementary data to this article can be found online at https://doi.org/10.1016/j.mtbio.2022.100531.

References

[1] S. Yan, P. Zhao, T. Yu, N. Gu, Current applications and future prospects of nanotechnology in cancer immunotherapy, Cancer Biol Med 16 (3) (2019) 486–497, https://doi.org/10.20892/j.issn.2095-3941.2018.0493.

[2] D.N. Khalil, E.L. Smith, R.J. Brentjens, J.D. Wolchok, The future of cancer treatment: immunomodulation, CARs and combination immunotherapy, Nat. Rev. Clin. Oncol. 13 (5) (2016) 273–290, https://doi.org/10.1038/nrclinonc.2016.25.

[3] N. Budimir, G.D. Thomas, J.S. Dolina, S. Salek-Ardakani, Reversing T-cell exhaustion in cancer: lessons learned from PD-1/PD-L1 immune checkpoint blockade, Cancer Immunol Res 10 (2) (2022) 146–153, https://doi.org/10.1158/2326-6066.CIR-21-0515.

[4] F. Petitprez, M. Meylan, A. de Reynies, C. Sautes-Fridman, W.H. Fridman, The tumor microenvironment in the response to immune checkpoint blockade therapies, Front. Immunol. 11 (2020) 784, https://doi.org/10.3389/fimmu.2020.00784.

[5] B. Seliger, Basis of PD1/PD-L1 therapies, J. Clin. Med. 8 (12) (2019), https://doi.org/10.3390/jcm8122168.

[6] Z. Li, G. Sun, G. Sun, Y. Cheng, L. Wu, Q. Wang, C. Lv, Y. Zhou, Y. Xia, W. Tang, Various uses of PD1/PD-L1 inhibitor in oncology: opportunities and challenges, Front. Oncol. 11 (2021), 771335, https://doi.org/10.3389/fonc.2021.771335.

[7] Y. Du, D. Zhang, Y. Wang, M. Wu, C. Zhang, Y. Zheng, A. Zheng, X. Liu, A highly stable multifunctional aptamer for enhancing antitumor immunity against hepatocellular carcinoma by blocking dual immune checkpoints, Biomater. Sci. 9 (11) (2021) 4159–4168, https://doi.org/10.1039/d0bm02210a.

[8] D. Zhang, Z. Lin, M. Wu, Z. Cai, Y. Zheng, L. He, Z. Li, J. Zhou, L. Sun, G. Chen, Y. Zeng, J. Li, J. Liu, H. Yang, X. Liu, Cytosolic delivery of thiolated neoantigen nano-vaccine combined with immune checkpoint blockade to boost anti-cancer T cell immunity, Adv. Sci. 8 (6) (2021) 2003504, https://doi.org/10.1002/advs.202003504.

[9] A.J. Korman, S.C. Garrett-Thomson, N. Lonberg, The foundations of immune checkpoint blockade and the ipilimumab approval decennial, Nat. Rev. Drug Discov. 21 (7) (2022) 509–528, https://doi.org/10.1038/s41573-021-00345-8.

[10] D. Schadendorf, F.S. Hodi, C. Robert, J.S. Weber, K. Margolin, O. Hamid, D. Patt, T.T. Chen, D.M. Berman, J.D. Wolchok, Pooled analysis of long-term survival data from phase II and phase III trials of ipilimumab in unresectable or metastatic melanoma, J. Clin. Oncol. 33 (17) (2015) 1889–1894, https://doi.org/10.1200/JCO.2014.56.2736.

[11] J. Weber, M. Mandala, M. Del Vecchio, H.J. Gogas, A.M. Arance, C.L. Cowey, S. Dalle, M. Schenker, V. Chiarion-Sileni, I. Marquez-Rodas, J.J. Grob, M.O. Butler, M.R. Middleton, M. Maio, V. Atkinson, P. Queirolo, R. Gonzalez, R.R. Kudchadkar, M. Smylie, N. Meyer, L. Mortier, M.B. Atkins, G.V. Long, S. Bhatia, C. Lebbe, P. Rutkowski, K. Yokota, N. Yamazaki, T.M. Kim, V. de Pril, J. Sabater, A. Qureshi, J. Larkin, P.A. Ascierto, C. CheckMate, Adjuvant nivolumab versus ipilimumab in resected stage III or IV melanoma, N. Engl. J. Med. 377 (19) (2017) 1824–1835, https://doi.org/10.1056/NEJMoa1709030.

[12] L.L. Huang, W. Nie, J. Zhang, H.Y. Xie, Cell-membrane-based biomimetic systems with bioorthogonal functionalities, Acc. Chem. Res. 53 (1) (2020) 276–287, https://doi.org/10.1021/acs.accounts.9b00559.

[13] S. Tan, T. Wu, D. Zhang, Z. Zhang, Cell or cell membrane-based drug delivery systems, Theranostics 5 (8) (2015) 863–881, https://doi.org/10.7150/thno.11852.

[14] C. Xu, D. Ju, X. Zhang, Cell membrane-derived vesicle: a novel vehicle for cancer immunotherapy, Front. Immunol. 13 (2022), 923598, https://doi.org/10.3389/fimmu.2022.923598.

[15] C. Yang, Y. Ming, K. Zhou, Y. Hao, D. Hu, B. Chu, X. He, Y. Yang, Z. Qian, Macrophage membrane-camouflaged shRNA and doxorubicin: a pH-dependent release system for melanoma chemo-immunotherapy, Research 2022 (2022), 9768687, https://doi.org/10.34133/2022/9768687.

[16] H. Pan, M. Zheng, A. Ma, L. Liu, L. Cai, Cell/bacteria-based bioactive materials for cancer immune modulation and precision therapy, Adv. Mater. 33 (50) (2021), https://doi.org/10.1002/adma.202100241.

[17] J. Xiong, M. Wu, J. Chen, Y. Liu, Y. Chen, G. Fan, Y. Liu, J. Cheng, Z. Wang, S. Wang, Y. Liu, W. Zhang, Cancer-erythrocyte hybrid membrane-camouflaged magnetic nanoparticles with enhanced photothermal-immunotherapy for ovarian cancer, ACS Nano 15 (12) (2021) 19756–19770, https://doi.org/10.1021/acsnano.1c07180.

[18] P. Yu, D. Zheng, C. Zhang, M. Wu, X. Liu, Protocol to prepare functional cellular nanovesicles with PD1 and TRAIL to boost antitumor response, STAR Protoc 2 (1) (2021), 100324, https://doi.org/10.1016/j.xpro.2021.100324.

[19] L. Rao, L. Wu, Z. Liu, R. Tian, G. Yu, Z. Zhou, K. Yang, H.G. Xiong, A. Zhang, G.T. Yu, W. Sun, H. Xu, J. Guo, A. Li, H. Chen, Z.J. Sun, Y.X. Fu, X. Chen, Hybrid cellular membrane nanovesicles amplify macrophage immune responses against cancer recurrence and metastasis, Nat. Commun. 11 (1) (2020) 4909, https://doi.org/10.1038/s41467-020-18626-y.

[20] N. Wang, C. Liu, Z. Lu, W. Yang, L. Li, S. Gong, T. He, C. Ou, L. Song, M. Shen, Q. Wu, C. Gong, Multistage sensitive NanoCRISPR enable efficient intracellular disruption of immune checkpoints for robust innate and adaptive immune coactivation, Adv. Funct. Mater. 30 (45) (2020), https://doi.org/10.1002/adfm.202004940.

[21] M. Wu, D. Zheng, D. Zhang, P. Yu, L. Peng, F. Chen, Z. Lin, Z. Cai, J. Li, Z. Wei, X. Lin, J. Liu, X. Liu, Converting immune cold into hot by biosynthetic functional vesicles to boost systematic antitumor immunity, iScience 23 (7) (2020), 101341, https://doi.org/10.1016/j.isci.2020.101341.

[22] P. Zhang, L. Zhang, Z. Qin, S. Hua, Z. Guo, C. Chu, H. Lin, Y. Zhang, W. Li, X. Zhang, X. Chen, G. Liu, Genetically engineered liposome-like nanovesicles as active targeted transport platform, Adv. Mater. 30 (7) (2018), https://doi.org/10.1002/adma.201705350.

[23] X. Zhang, C. Wang, J. Wang, Q. Hu, B. Langworthy, Y. Ye, W. Sun, J. Lin, T. Wang, J. Fine, H. Cheng, G. Dotti, P. Huang, Z. Gu, PD-1 blockade cellular vesicles for cancer immunotherapy, Adv. Mater. 30 (22) (2018), e1707112, https://doi.org/10.1002/adma.201707112.

[24] X. Zhang, J. Wang, Z. Chen, Q. Hu, C. Wang, J. Yan, G. Dotti, P. Huang, Z. Gu, Engineering PD-1-presenting platelets for cancer immunotherapy, Nano Lett. 18 (9) (2018) 5716–5725, https://doi.org/10.1021/acs.nanolett.8b02321.

[25] D.C. Hinshaw, L.A. Shevde, The tumor microenvironment innately modulates cancer progression, Cancer Res. 79 (18) (2019) 4557–4566, https://doi.org/10.1158/0008-5472.CAN-18-3962.

[26] Q.V. Le, J. Suh, Y.K. Oh, Nanomaterial-based modulation of tumor microenvironments for enhancing chemo/immunotherapy, AAPS J. 21 (4) (2019) 64, https://doi.org/10.1208/s12248-019-0333-y.

[27] B. Wang, Q. Zhao, Y. Zhang, Z. Liu, Z. Zheng, S. Liu, L. Meng, Y. Xin, X. Jiang, Targeting hypoxia in the tumor microenvironment: a potential strategy to improve cancer immunotherapy, J. Exp. Clin. Cancer Res. 40 (1) (2021) 24, https://doi.org/10.1186/s13046-020-01820-7.

[28] J. Li, Y. Ma, T. Zhang, K.K. Shung, B. Zhu, Recent advancements in ultrasound transducer: from material strategies to biomedical applications, BME Frontiers 2022 (2022) 1–19, https://doi.org/10.34133/2022/9764501.

[29] C.S. Yuan, Z.W. Deng, D. Qin, Y.Z. Mu, X.G. Chen, Y. Liu, Hypoxia-modulatory nanomaterials to relieve tumor hypoxic microenvironment and enhance immunotherapy: where do we stand? Acta Biomater. 125 (2021) 1–28, https://doi.org/10.1016/j.actbio.2021.02.030.

[30] M. Hao, B. Chen, X. Zhao, N. Zhao, F.-J. Xu, Organic/inorganic nanocomposites for cancer immunotherapy, Mater. Chem. Front. 4 (9) (2020) 2571–2609, https://doi.org/10.1039/d0qm00323a.

[31] H. Lin, Y. Chen, J. Shi, Nanoparticle-triggered in situ catalytic chemical reactions for tumour-specific therapy, Chem. Soc. Rev. 47 (6) (2018) 1938–1958, https://doi.org/10.1039/c7cs00471k.

[32] J. Mujtaba, J. Liu, K.K. Dey, T. Li, R. Chakraborty, K. Xu, D. Makarov, R.A. Barmin, D.A. Gorin, V.P. Tolstoy, G. Huang, A.A. Solovev, Y. Mei, Micro-bio-chemo-mechanical-Systems: micromotors, microfluidics, and nanozymes for biomedical applications, Adv. Mater. 33 (22) (2021), e2007465, https://doi.org/10.1002/adma.202007465.

[33] B. Xu, Y. Cui, W. Wang, S. Li, C. Lyu, S. Wang, W. Bao, H. Wang, M. Qin, Z. Liu, W. Wei, H. Liu, Immunomodulation-Enhanced nanozyme-based tumor catalytic therapy, Adv. Mater. 32 (33) (2020), e2003563, https://doi.org/10.1002/adma.202003563.

[34] Y. Zhao, X. Xiao, M. Zou, B. Ding, H. Xiao, M. Wang, F. Jiang, Z. Cheng, P. Ma, J. Lin, Nanozyme-initiated in situ cascade reactions for self-amplified biocatalytic immunotherapy, Adv. Mater. 33 (3) (2021), e2006363, https://doi.org/10.1002/adma.202006363.

[35] Y. Yang, K. Hu, P. Zhang, P. Zhou, X. Duan, H. Sun, S. Wang, Manganese-based micro/nanomotors: synthesis, motion, and applications, Small 17 (50) (2021), e2100927, https://doi.org/10.1002/smll.202100927.

[36] J. Wen, K. Yang, S. Sun, MnO₂-Based nanosystems for cancer therapy, Chem. Commun. 56 (52) (2020) 7065–7079, https://doi.org/10.1039/d0cc02782k.

[37] Z. Zhang, Y. Ji, Nanostructured manganese dioxide for anticancer applications: preparation, diagnosis, and therapy, Nanoscale 12 (35) (2020) 17982–18003, https://doi.org/10.1039/d0nr04067c.

[38] T. Lin, X. Zhao, S. Zhao, H. Yu, W. Cao, W. Chen, H. Wei, H. Guo, O₂-generating MnO₂ nanoparticles for enhanced photodynamic therapy of bladder cancer by ameliorating hypoxia, Theranostics 8 (4) (2018) 990–1004, https://doi.org/10.7150/thno.22465.

[39] Y. Liu, Y. Pan, W. Cao, F. Xia, B. Liu, J. Niu, G. Alfranca, X. Sun, L. Ma, J.M. de la Fuente, J. Song, J. Ni, D. Cui, A tumor microenvironment responsive biodegradable CaCO₃/MnO₂- based nanoplatform for the enhanced photodynamic therapy and improved PD-L1 immunotherapy, Theranostics 9 (23) (2019) 6867–6884, https://doi.org/10.7150/thno.37586.

[40] G. Yang, L. Xu, Y. Chao, J. Xu, X. Sun, Y. Wu, R. Peng, Z. Liu, Hollow MnO₂ as a tumor-microenvironment-responsive biodegradable nano-platform for combination therapy favoring antitumor immune responses, Nat. Commun. 8 (1) (2017) 902, https://doi.org/10.1038/s41467-017-01050-0.

[41] W. Zhu, Z. Dong, T. Fu, J. Liu, Q. Chen, Y. Li, R. Zhu, L. Xu, Z. Liu, Modulation of hypoxia in solid tumor microenvironment with MnO₂ nanoparticles to enhance photodynamic therapy, Adv. Funct. Mater. 26 (30) (2016) 5490–5498, https://doi.org/10.1002/adfm.201600676.

[42] M.Z. Zou, W.L. Liu, C.X. Li, D.W. Zheng, J.Y. Zeng, F. Gao, J.J. Ye, X.Z. Zhang, A multifunctional biomimetic nanoplatform for relieving hypoxia to enhance chemotherapy and inhibit the PD-1/PD-L1 Axis, Small 14 (28) (2018), e1801120, https://doi.org/10.1002/smll.201801120.

[43] M. Lv, M. Chen, R. Zhang, W. Zhang, C. Wang, Y. Zhang, X. Wei, Y. Guan, J. Liu, K. Feng, M. Jing, X. Wang, Y.C. Liu, Q. Mei, W. Han, Z. Jiang, Manganese is critical for antitumor immune responses via cGAS-STING and improves the efficacy of clinical immunotherapy, Cell Res. 30 (11) (2020) 966–979, https://doi.org/10.1038/s41422-020-00395-4.

[44] L. Hou, C. Tian, Y. Yan, L. Zhang, H. Zhang, Z. Zhang, Manganese-based nanoactivator optimizes cancer immunotherapy via enhancing innate immunity, ACS Nano 14 (4) (2020) 3927–3940, https://doi.org/10.1021/acsnano.9b06111.

[45] C. Jia, Y. Guo, F.G. Wu, Chemodynamic therapy via Fenton and fenton-like nanomaterials: strategies and recent advances, Small 18 (6) (2022), e2103868, https://doi.org/10.1002/smll.202103868.

[46] L.S. Lin, J. Song, L. Song, K. Ke, Y. Liu, Z. Zhou, Z. Shen, J. Li, Z. Yang, W. Tang, G. Niu, H.H. Yang, X. Chen, Simultaneous fenton-like ion delivery and glutathione depletion by MnO₂ -based nanoagent to enhance chemodynamic therapy, Angew Chem. Int. Ed. Engl. 57 (18) (2018) 4902–4906, https://doi.org/10.1002/anie.201712027.

[47] X. Meng, X. Zhang, M. Liu, B. Cai, N. He, Z. Wang, Fenton reaction-based nanomedicine in cancer chemodynamic and synergistic therapy, Appl. Mater. Today 21 (2020), https://doi.org/10.1016/j.apmt.2020.100864.

[48] L. Xie, G. Wang, W. Sang, J. Li, Z. Zhang, W. Li, J. Yan, Q. Zhao, Y. Dai, Phenolic immunogenic cell death nanoinducer for sensitizing tumor to PD-1 checkpoint blockade immunotherapy, Biomaterials 269 (2021), 120638, https://doi.org/10.1016/j.biomaterials.2020.120638.

[49] J. Li, S. Wang, X. Lin, Y. Cao, Z. Cai, J. Wang, Z. Zhang, X. Liu, M. Wu, C. Yao, Red blood cell-mimic nanocatalyst triggering radical storm to augment cancer immunotherapy, Nano-Micro Lett. 14 (1) (2022) 57, https://doi.org/10.1007/s40820-022-00801-z.

[50] H. Dai, Q. Fan, C. Wang, Recent Applications of Immunomodulatory Biomaterials for Disease Immunotherapy, Exploration, 2022, https://doi.org/10.1002/exp.20210157.